Automation in Construction 137 (2022) 104202

Contents lists available at ScienceDirect

Automation in Construction

journal homepage: www.elsevier.com/locate/autcon

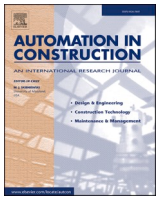

3D printed cement-based repairs and strain sensors

Christos Vlachakis, Jack McAlorum, Marcus Perry *

Civil and Environmental Engineering, University of Strathclyde, Glasgow, United Kingdom

ARTICLE INFO

Keywords:
Printed sensors
Cement printing
Additive manufacturing
Alkali activated materials
Multifunctional materials
Concrete repairs

ABSTRACT

This paper presents 3D printed strain sensors based on alkali activated cement repairs, demonstrating a fixed-cost method for remotely deploying a combined monitoring and maintenance technology for construction. Experimental protocols to quantitatively assess the compatibility of cements and 3D printing processes are defined and investigated in this paper. The strain sensing response of printed self-sensing cements is then investigated under compression and tension by monitoring changes in material electrical impedance. Gauge factors for self-sensing repairs printed onto concrete substrates were 8.6 ± 1.6 under compression, with an average adhesion strength of 0.6 MPa between printed repair and concrete substrate. Gauge factors for repairs printed onto glass fibre reinforced polymers were 38.4 ± 21.6 under tension: more variable than for concrete substrates due to incompatibilities between the repair and the polymer substrate. This proof-of-concept is a step towards monitoring and maintenance methods that are more compatible with the time and cost drivers of modern construction.

1. Introduction

Civil asset managers have a clear need for tools that reduce the costs and risks of concrete monitoring and maintenance, so that they can ensure the continued resilience of ageing critical infrastructure. Self-sensing cements may provide one pathway to improving efficiency, as they act as traditional concrete binders and repairs [1,2] while also encoding local changes in strain [3], damage [4], temperature [5] and moisture [6] as measurable shifts in their electrical impedance. Alkali activated materials (AAM) are a low-carbon alternative to ordinary Portland cements (OPC) that are particularly well-suited to self-sensing, as their inherently high electrical conductivity ($\sim 10^{-6}$ S/cm), negates the need to use electrically conductive additives [7–9].

Regardless of the material fabrication method, a self-sensing cementitious material needs to be deployed to produce one of the following:

i) **Self-sensing structural element:** Here, the electrically conductive AAM/OPC matrix is mixed with aggregates to produce a self-sensing concrete cube or beam [10–12];
ii) **Embedded cement-based sensor:** Pre-fabricated cement-based sensors (typically a small cube or beam) are embedded inside a larger cement-based element (such as a larger cube, beam or column) during casting [13–15]
iii) **Retrofitted sensing coating:** Coatings are deployed, usually manually, onto existing concrete substrates [3,5,16,17]. Measurands such as strain are transferred from the substrate to the coating, with strain transfer efficiency mainly governed by the degree of adhesion between the two materials [18], and coating thickness [16].

In high- and upper-middle- income countries, most concrete infrastructure has already been built. This means that self-sensing coatings and repairs for existing concrete structures have larger potential market than new self-sensing construction elements or semi-destructively embedded sensor architectures. However, as with all sensors and novel materials, the retrofit of self-sensing AAM/OPC repair poses practical challenges for industrialists. Manual deployment in a construction context is expensive, places workers at risk, and leads to variable sensing performance due to human errors in deployment. Additive manufacturing (more colloquially known as 3D printing) could provide the answer to this deployment problem, as it allows for remote, automated and repeatable, deployment of materials at fixed cost [19–22].

Despite this promise, there remain research questions in how 3D printing processes for cementitious materials can be optimised for repair printing in a way that allows for optimisation and comparison across independent studies. The first objective of this paper is therefore to outline and demonstrate a new set of adaptable experimental protocols that allow the performance of printed cementitious materials to be

* Corresponding author.
E-mail address: m.perry@strath.ac.uk (M. Perry).

https://doi.org/10.1016/j.autcon.2022.104202
Received 29 September 2021; Received in revised form 26 January 2022; Accepted 6 March 2022
Available online 14 March 2022

stated in more quantifiable terms. Following this, our second objective is to provide a detailed characterisation of our printed repair's strain-sensing performance, with a particular focus on repeatability and hysteresis in the sensing response.

The work outlined here supports a technology which merges the benefits of self-sensing AAM repair materials with additive manufacturing, in doing so, we demonstrate for the first time, 3D printed patches. This technology may in future support the de-risked, remote, and potentially autonomous deployment of strains sensors and repairs in the construction sector primarily in areas of hazardous access such as locations at height, or within nuclear plants and in the oil and gas industry.

2. Background theory and methods

2.1. Alkali-activated materials

Alkali-activated materials (AAM) are formulated by mixing aluminosilicate precursors (such as metakaolin, fly ash or blast-furnace slag) with an alkaline activator solution comprised of a mix of potassium (K^+) or sodium (Na^+) based silicates and hydroxides [23]. The alkali metal ions introduced by the activator solution are the primary source of the self-sensing capabilities of AAM binders, as they promote a high electrolytic conductivity that can be monitored via electrodes embedded in the sample.

Strain sensing in cementitious materials is attributed to ionic conduction (migration) and electronic conduction. Ionic conduction is a result of the movement of free ions in the matrix's pore solution. In AAM, ionic conductivity occurs due to movement of the alkali cations (Na^+ or K^+) in the matrix that charge balance the aluminium (III) in the tetrahedral AlO_4^- coordination. It has been posited that the distances the ions are required to travel under mechanical loading are altered resulting in a change in electrical properties [7,8].

Electronic conduction is a result of the movement of electrons in the conductive filler added to the cementitious matrix. If the content of the conductive filler does not form a continuous network in the matrix (i.e. below the percolation threshold), then sensing is a result of electron hopping (tunnelling effect) between filler. When the quantity of filler is able to form a continuous network in the matrix, sensing is a result of the conductive network formed. As load is applied, the path the electrical current follows in both cases changes, thus impacting the electrical response of the binder [24].

In this work, kaolin originating from Southwest England, UK, was calcined at 800 °C for 2 h in an electric furnace to produce metakaolin. This metakaolin was mixed at a 95:5 weight ratio with 90%-densified silica fume to produce a precursor. The chemical compositions of precursor materials, measured via x-ray diffraction [5], are shown in Table 1. PVA fibres of 3 mm length were added to the precursor (0.5 wt %) to reduce drying shrinkage [25] and to increase shape stability during printing [26].

Sodium silicate (27.8% SiO_2 and 8.5% Na_2O) and sodium hydroxide (10 M) were mixed at a mass ratio of 2 to make the activator solution. The activator was poured into the dry components and mixed for 5 min until a homogenous mix was achieved. The final precursor to solution ratio was 0.90, and the density of the final uncured mix was 1.73 g/mL.

Table 1
– Chemical composition of precursor components.

Material	SiO_2 (%)	Al_2O_3 (%)
Kaolin	47	38
Metakaolin	87%	
Silica fume	92.85	0.27

2.2. 3D printing of AAM

The 3D printing set up is similar to that described in our previous work [5]. Briefly, a screw cavity extruder fitted with a nozzle of size 18G (0.84 mm) was mounted onto a commercial 3D printer with an x-y gantry axis (Fig. 1). The uncured AAM was inserted into the syringe barrel and a pressure of 2 bar was applied to feed the material from the cartridge into the dispenser. The flowrate of extrusion was 2 mL/min, and the print speed was 30 mm/s.

A 3D CAD file of the intended objects was exported in stereolithography (STL) file format. Slicer software (Slic3r) was used to generate the required G-Code from the STL file, which defines the print paths and extrusion rates. Adjustments to the G-Code to include required time gaps were made by editing the code directly.

Two types of objects were printed for this investigation, buildability rings (see Section 3.3) and patches/overlays for adhesion and sensor testing (outlined in Sections 3.4 and 4.3 respectively). Fig. 2 presents a typical data file for a buildability ring and the overlay. Buildability rings were comprised of up to 10 layers. Patches consisted of two layers, each of layer height 0.6 mm, deposited with a rectilinear infill density of 100% and a 90° crosshatched infill pattern. A single perimeter was also added to close potential gaps at the patch's edges caused by the infill path to improve interlocking between the infill and the outer shell [27].

3. Parameters 3D printing cement overlays

The work in this paper originally had the single aim of demonstrating the printing of strain-sensing AAM repairs. Before we could achieve this, however, we discovered a need to assess and quantify the properties of our AAM mix so that we could optimise its mix design and printing parameters. To this end, we have modified a method originally put forward by Le et al. [28] and later Kazemian et al. [29], to produce four essential parameters to assess the 3D printing of cement overlays:

i. **Extrudability**: The ability of a mix to be continuously extruded as a continuous filament from a dispensing unit.
ii. **Printability window**: Time limit in which the mix is printable and no blockage occurs.
iii. **Buildability**: The ability of a material to maintain its self-weight and the weight of subsequent layers without noticeable deformation.
iv. **Adhesion**: The bond strength achieved between the printed material and the substrate.

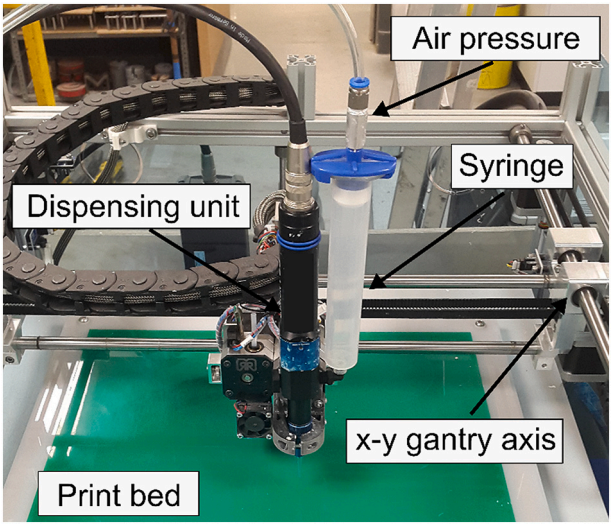

Fig. 1. – Cavity dispenser mounted onto x-y gantry axis.

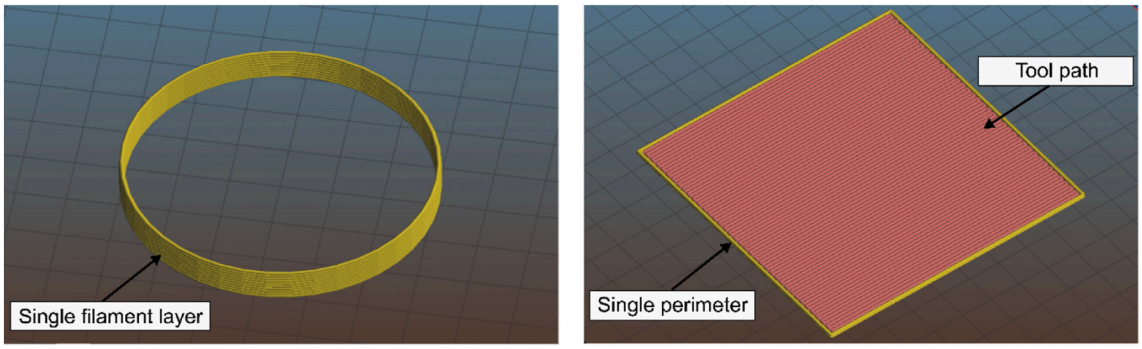

Fig. 2. – G-Code representation of a) buildability ring and b) overlay for concrete substrate.

In this study the aim was to quantitively portray these parameters (in particular, extrudability and buildability) and convert them to experimentally measurable metrics that can be optimised.

Measurements of electrical impedance are also required in the present work to assess whether the printed specimen can be electrically interrogated, but this is discussed in more detail in Section 4.

3.1. Extrudability

Extrudability was broken down into two phases, both of which provide a true/false result. During phase 1, we test whether filament can be extruded for 10 s by the dispensing unit. The second phase involves printing three lines of filament with a length of 200 mm (each line separated by 4 mm). The 200 mm length was chosen to approximately match the intended lengths of features in our final application. If these longer printed lines were free from defects and had a consistent shape, then the mix was deemed extrudable.

The mix design described in Section 2.1 (with 0.5 wt% 3 mm PVA fibres) passed the phase 1 extrudability test. Other mixes which used higher quantities of PVA fibre (e.g. 1 wt%), longer PVA fibres (e.g. 6 mm), or stiffer fibres (e.g. carbon- or polypropylene fibres) did not pass the phase 1 test using our particular printing set up, so were discarded from further assessment.

Fig. 3 depicts the outcome of the phase 2 test for the successful mix design candidate. As shown, the three lines maintained a fairly consistent shape and were free from major defects. Slight variations in extruded thickness resulted from variations in levelling and entrapped air in the cement mix. This extrudability test could be improved in future work by imaging these extruded lines or by measuring their mass to better quantify variations in deposition rates and line thickness.

3.2. Printability window

The printability window is a parameter that determines how long a mix can be extruded without significant discontinuities. This test is essentially an extension of the extrudability test: three lines with a length of 200 mm (4 mm spacing) were printed every 10 min until major discontinuities were observed.

Fig. 3. – Extrudability assessment of mix design by printing three 200 mm lines.

Fig. 4 presents the results of the printability window test with the mix and printing parameters described in Section 2. As shown, the printability window is 120 min, as the filament is extrudable in a consistent manner for this duration. Small gaps that do appear are primarily due to residual air bubbles in the filament. Beyond this 120 min time frame, our mix suddenly became difficult to extrude, as it hardened and clogged the dispenser due to increasing viscosity over time.

For completeness, the open time of the AAM mix was measured using a Vicat needle as outlined in BS EN 196–3:2016 [30]. The initial and final setting time of the mix were recorded as 16 h and 20 h respectively. This setting time is long compared to mixes used in most printing applications in the literature, but mixes with prolonged setting times [26] are still usable. In general the setting time of mixes is short (less than an hour) in mixes which have higher solid contents, fillers and thickening agents [31,32].

The ongoing challenge in cementitious 3D printing is understanding how parameters like open time or workability (measured using a standard slump test) can be used to optimise a 3D printing process in which there are many coupled variables. These parameters are perhaps better suited to conventional concrete mix design. Open time is, furthermore the only printing parameter directly referring to “time” in Le et al.’s original set of printing parameters [28]. Diggs-McGee et al. [33] conducted an extensive study to define the different categories of time in 3D printing. Time was classified as total construction time, print time of layer, delay time and elapsed time of layer. Most studies primarily focus on the total time to construct an object without considering potential faults and maintenance requirements in printing. This is what we have

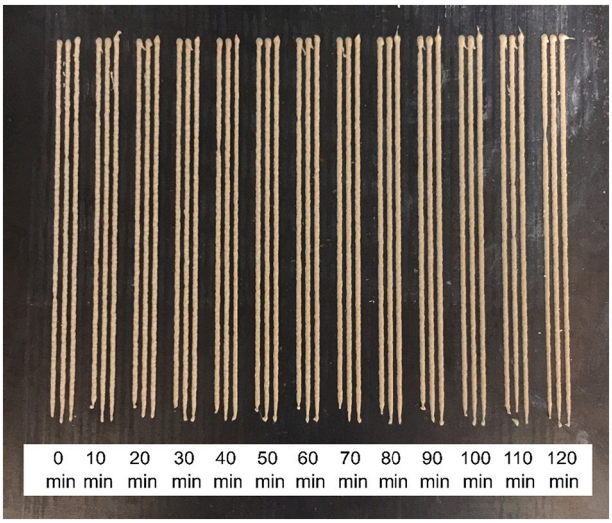

Fig. 4. – Printability window test for 120 min at 10 min intervals.

attempted to address in the present experimental work.

3.3. Buildability

Buildability in this work has been defined by extruding cylinders, or "buildability rings", with a diameter of 60 mm, as shown in Fig. 5. We can then define the buildability as:

$$\text{Buildability } (\%) = \frac{\text{Actual height of printed object}}{\text{Design height}} \times 100 \quad (1)$$

In this work, buildability rings were printed with a time gap of 1 min between printed layers. Ten rings were printed for each test and 10 height measurements were made for each ring to assess the buildability as a function of the number of printed layers.

Fig. 6 shows the buildability for the mix printed with a time gap of 1 min between layers. Buildability starts at 98% but can drop as low 73% after 10 layers. This signals that the previous layers are unable to fully support the weight of the newly deposited layers, especially if they are not given much time to harden. This results in deformation and subsequently incorrect filament deposition due to the increasing head distance. The maximum recommended deformation allowed in buildability and shape retention tests ranges between 80 and 90% [34–36]. If we arbitrarily select a cut-off of 95%, then Fig. 6 suggests that we should not print any more than 2 layers. If required, buildability can be increased by expanding the time gap between layers [37]. Large time delays though can be counterproductive as they can lead to excessively long print runs.

Note that when investigating the buildability, it is important to keep a constant head distance between all objects. Different head distances can lead to different quality objects and ultimately different heights. Fig. 7 presents four supposedly identical rings that have been printed with different head distances. As can be seen, as the nozzle's distance from the bed increases, the quality of the printed object decreases. The head distance should be kept constant (equal to the layer height) during buildability tests to ensure consistency.

As pointed out by Nerella et al. [38], when talking about buildability, the allowed deformations and tolerances should be based on the end application, to avoid the risk of overdesigning. In the current application, the intention is to produce self-sensing coatings on substrates. Deformation is allowable in this application as coatings are required to spread onto the concrete surface and anchor into the concrete capillaries to achieve a greater bond [39]. The mix and methods that we outline here will not be suitable for constructing structural elements. Indeed, the application discussed in the present work could be considered as 2.5D printing due to the relatively low thickness of the layers [40], although the terminology used does not affect our requirement to develop an quantifiable printing parameters.

Fig. 5. – Ten-layer printed buildability ring.

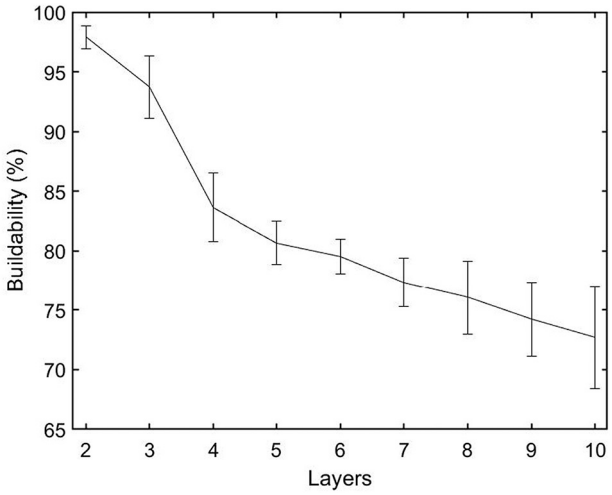

Fig. 6. –Buildability for rings between 2 and 10 layers with a time delay between layers of 1 min. Errors bars represent standard deviation of 10 measurements per sample for 10 samples.

3.4. Adhesion

In the present work, adhesion refers to adhesion between the printed patch, and the concrete substrate (rather than the inter-layer adhesion between printed layers [41]). Adhesion is required for a self-sensing cementitious patch as it affects strain transfer from the substrate to the sensor, and because the bond strength of the patches with the concrete is an indicator of their suitability for use as a repair material.

Double-layered 90 mm × 90 mm patches were printed onto 100 mm concrete cubes (as shown Fig. 10, concrete mix design C30-compressive strength of 30 MPa). The top layer of the concrete cube surface was removed with an electrical brush prior to printing to expose the aggregates to improve adhesion between the patch and the substrate [42], and the concrete substrate was also pre-wetted [43] to avoid liquid absorption from the concrete and thus excess liquid loss from the repair.

The bond strength of the printed AAM patches onto concrete was evaluated using a pull-off adhesion tester in accordance with BS EN 1542–1999 [44] at 6, 28 and 97 days after extrusion. The results, presented in Fig. 8 show no substantial change over the course of time. All coatings tested exhibited adhesive failure at the interface between the patch and the substrate. Overall the average bond strength of 0.6 MPa is low compared to manually deployed AAM repairs [25,45] but it is still within a serviceable range for a non-structural repair material. While it could be inferred that the layer-by-layer deposition may have affected the mechanical properties of the coatings [46], this could also be a result of the surface preparation technique. The mean surface roughness of the concrete after wire brushing (characterised using a Micro Epsilon Scan Control 2700–100) was 0.44–0.68 mm, which is relatively low compared to that achieved in other studies that employ more aggressive techniques like sandblasting [47].

4. Strain sensing characterisation methods

4.1. Overview

With a printable cement patch in hand, we proceed to characterise strain sensing performance. The following AAM overlays were printed for strain sensor characterisation:

- Large square patches of footprint 90 mm × 90 mm printed onto 100 mm side concrete cubes (as shown in Fig. 10).
- Small square patches of footprint 45 mm × 45 mm printed onto smaller 50 mm side concrete cubes.

Fig. 7. – Printed objects with different surface quality due head distance issues (head distance increases from left to right).

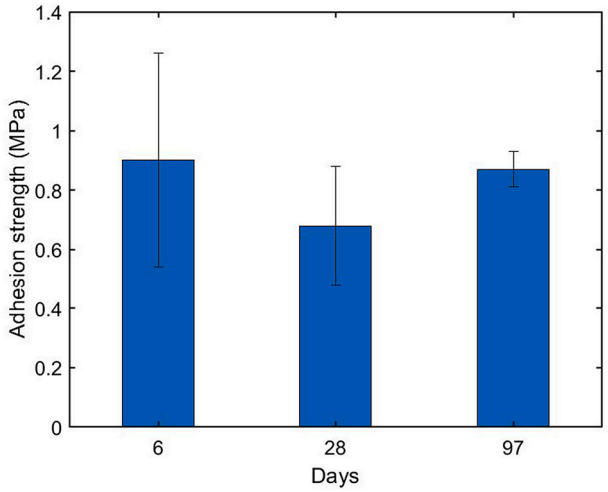

Fig. 8. – Adhesion strength of printed overlays at days 6, 28 & 97. Errors bars represent standard deviation of measurements for 3 samples.

- Rectangular patches of footprint 35 mm × 50 mm printed onto glass fibre reinforced polymer (GFRP) test pieces. Fig. 9 shows test piece dimensions and Fig. 11 shows a printed patch on a GFRP test piece under tensile testing.

GFRP was chosen as an alternative substrate for strain characterisation it is an electrically insulating material that can be tested under tension, and it presents a linear stress-strain response in the loading range investigated in this paper. The material properties of the GFRP substrate are listed in Table 2. While steel substrates are more traditionally used in tensile testing, complete electrical insulation between a steel substrate and an AAM layer is difficult to achieve. Current flow in a steel test piece (and indeed the grips of the tensile tester) would make these components part of the sensing system. AAM and GFRP do, however, have poor adhesion compatibility, so sand was epoxied onto the 'neck' of the tester (area between A × W in Fig. 9) prior to patches being printed in this region. This allowed the AAM patches to mechanically interlock with the sand.

Once patches were extruded onto substrates, stainless steel electrodes were inserted into the uncured AAM in the Van der Pauw (VDP) configuration [48], as shown in Fig. 10. Once electrodes were inserted,

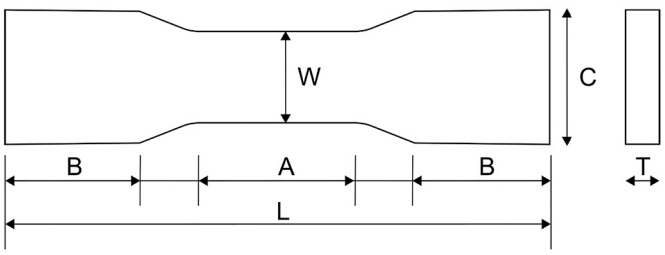

Fig. 9. GFRP test piece dimensions: A = 60 mm, B = 50 mm, C = 50 mm, L = 200 mm, T = 8 mm and W = 35 mm.

Table 2
– Manufacturer's values for properties of GFRP.

Tensile strength	Elongation	Density	Modulus of elasticity
160 MPa	3.5–5%	1.35 g/cm^3	5.5 GPa

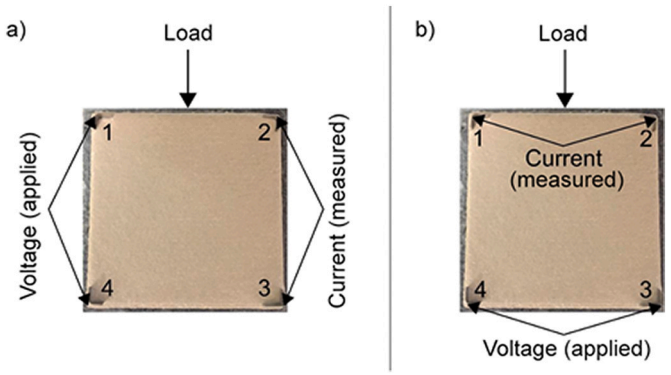

Fig. 10. – Large square patches printed onto concrete cubes. Images also show electrode orientation of patches: a) Layout 1 where measurement is parallel to applied load; b) Layout 2 where strain measurement is perpendicular to applied load.

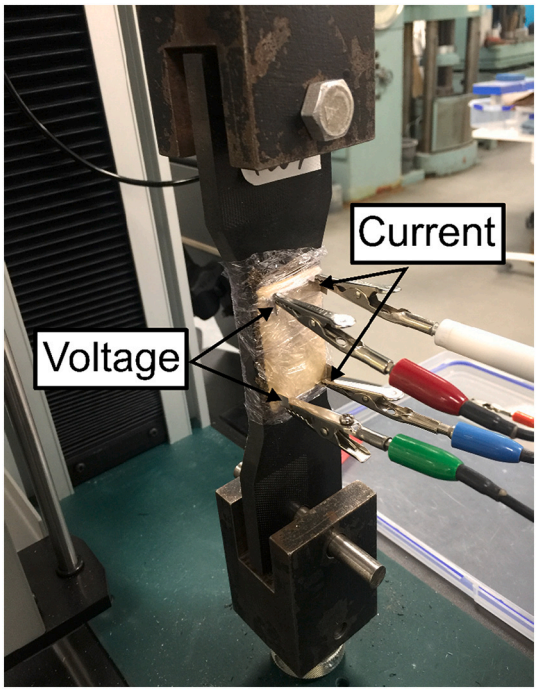

Fig. 11. GFRP test piece hosting 3D printed rectangular AAM patch under tensile testing and interrogation.

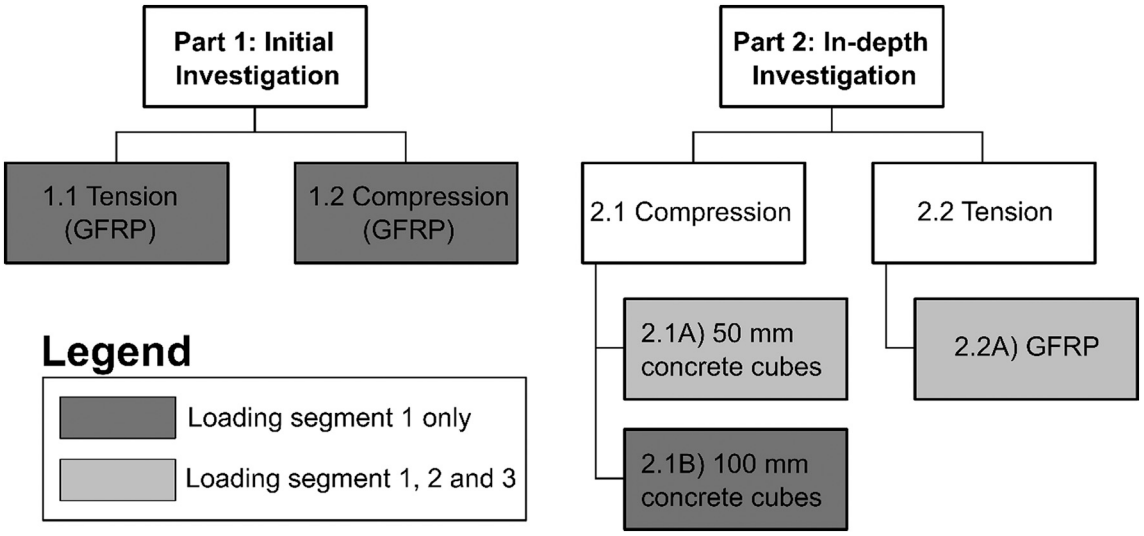

Fig. 12. – Summary of the five mechanical tests conducted in this work, and the loading segments that were investigated during each test.

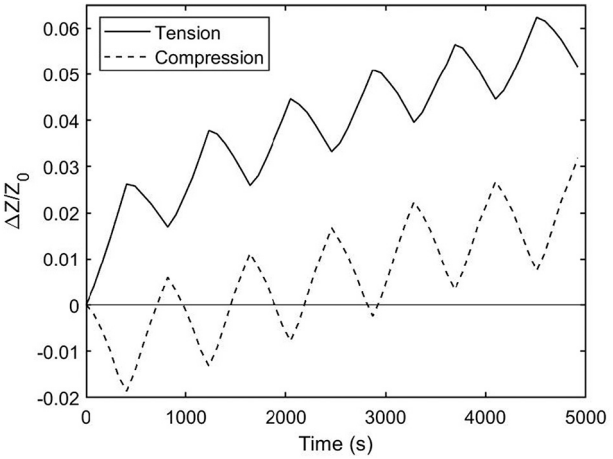

Fig. 13. – Compressive and tensile strain sensing behaviour of patches printed on GFRP during loading Segment 1.

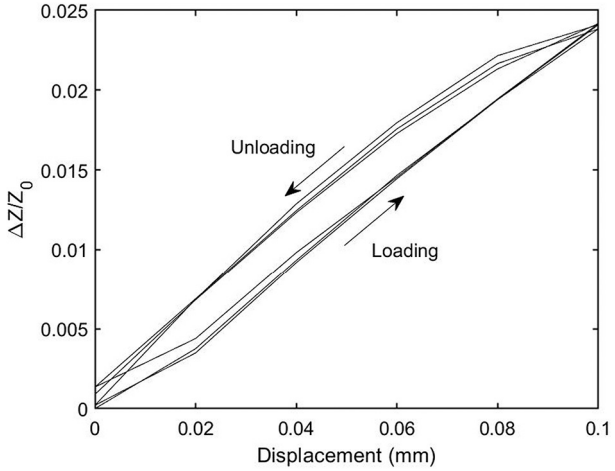

Fig. 15. – Fractional change in impedance versus applied displacement for 3 load cycles under tension for GFRP.

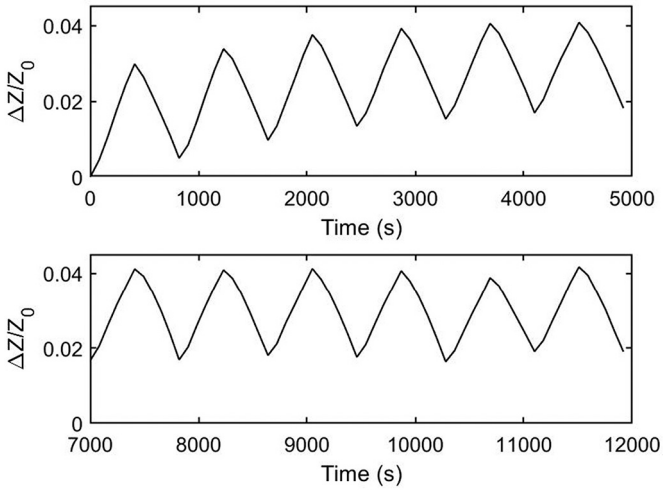

Fig. 14. – Sensing response of patch printed on GFRP under tension for (top) loading Segment 1 (cycles 1–6) and (bottom) loading Segment 3 (cycles 47–52).

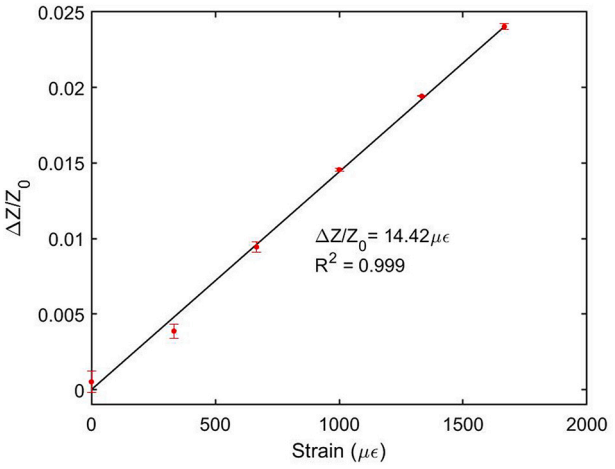

Fig. 16. – Averaged (over 3 load cycles) fractional change in impedance versus tensile strain for patch printed on GFRP.

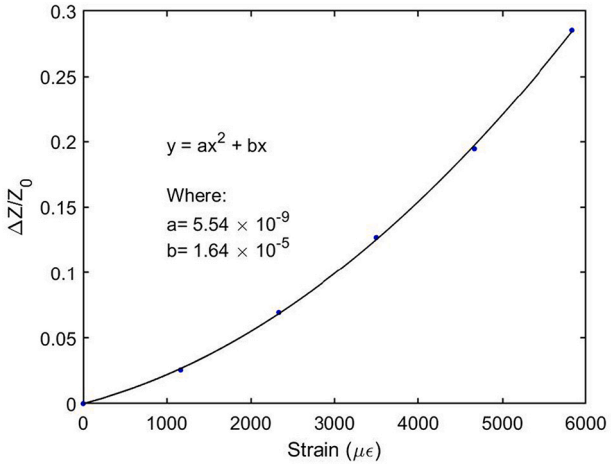

Fig. 17. – Nonlinear sensing response of patch printed on GFRP under high tensile strain.

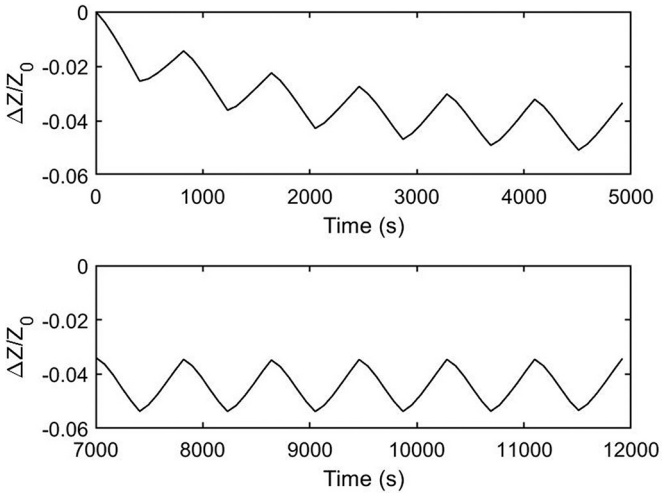

Fig. 18. – Sensing response of patch printed on 50 mm cube under compression for loading: (top) Segment 1 (cycles 1–6) and (bottom) loading Segment 3 (cycles 47–52).

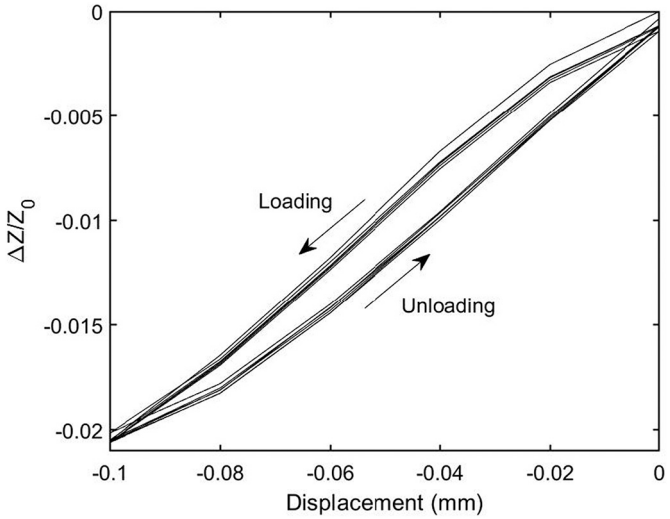

Fig. 19. – Fractional change in impedance versus applied displacement for 6 load cycles under compression for 50 mm concrete cube.

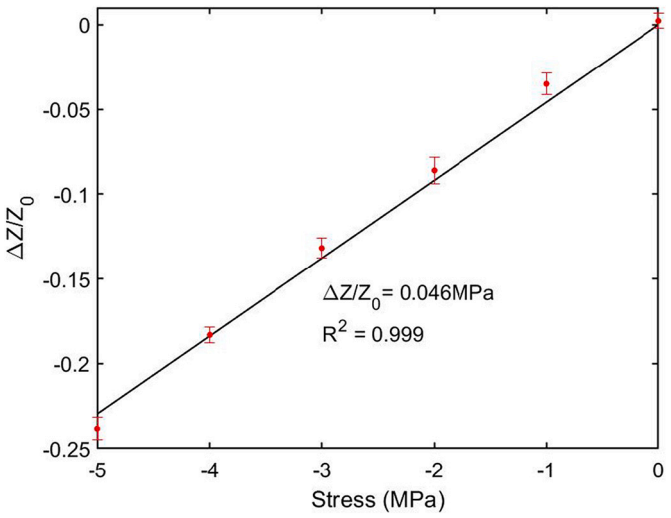

Fig. 20. – Average fractional change in impedance versus applied stress for 100 mm concrete cubes for 6 load cycles.

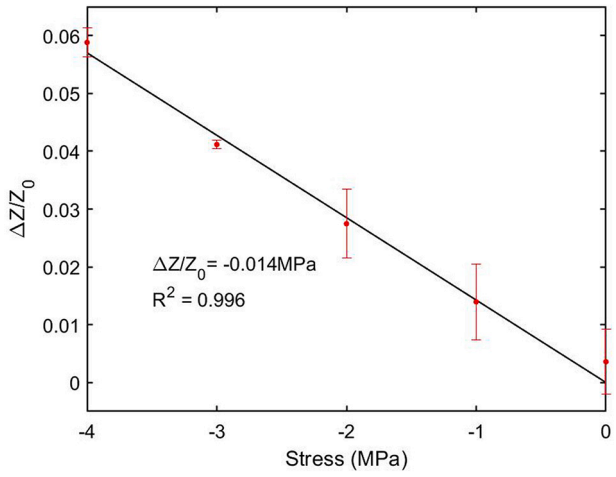

Fig. 21. – Average fractional change in impedance versus applied compressive stress for 100 mm concrete cubes interrogated using electrode layout 2.

samples were cured in containers at ambient temperature for 28 days.

4.2. Electrical impedance measurement

To prevent electrolysis at the electrodes, AAM samples are usually excited using an alternating voltage, *V(t)*. The resulting current response, *I(t)*, is measured and used to calculate the sample's impedance:

$$\frac{V(t)}{I(t)} = Z[cos(\varphi) + isin(\varphi)] = Ze^{i\varphi}, \quad (2)$$

where $Z = |\vec{Z}|$ is the impedance modulus or magnitude, and φ is the phase difference between the current and voltage. There have historically been studies that use direct current to interrogate AAM sensors (i.e. they measure the sample's electrical *resistance*, rather than its impedance). These studies risk inducing time-dependent changes in impedance due to interactions between alkali-metal ions and the electrodes.

While the VDP method provides an average measurement of patch impedance that is less sensitive to lead and contact resistances, the orientation of the electrical connections has important impacts for strain sensing [49]. To measure strain responses in the direction of the applied

load, the voltage and current should be applied and measured parallel to the applied load as shown in Fig. 10a (i.e. voltage is applied across electrodes 1 and 4 and current is measured across electrodes 2 and 3). This configuration is denoted 'Layout 1'. As part of a further investigation in this work, 'Layout 2' shown in Fig. 10b was also tested. In this configuration measurement is made perpendicular to the loading direction, so we may expect to measure strains induced by the Poisson effect.

During mechanical testing, AAM patch electrical impedance was interrogated using an impedance analyser in potentiostatic mode. Voltage excitations of amplitude 10 mV and frequency 5 kHz were applied, and three measurements of the current response were obtained at each load state. The average and standard deviation (error bar) value of the impedance modulus, Z, at each load state was then calculated.

The average initial impedance values for sensors applied onto concrete cubes (both 50 mm and 100 mm) and tensile pieces was 190 Ω and 3591 Ω respectively. It can be inferred that the type of substrate and the nature of the interface between the sensor and the substrate impacts impedance measurements.

4.3. Mechanical testing for sensor characterisation

4.3.1. Factors affecting strain sensing

The strain sensing performance of self-sensing cementitious materials is affected loading rates [50,51], temperatures during testing [15,52], moisture content of the sample [53–55] and filler content (when present) [10,56,57]. Most of these factors have only been investigated in OPC binders rather than in AAM. Nevertheless, previous studies on OPC were used to design the following constraints for mechanical testing in this work:

- Samples were removed from containers and placed next to the testing apparatus for 15 h to allow them to equilibrate with the testing environment prior to testing.
- Experiments were conducted in a stable environment at constant temperature and humidity of at 21.7 ± 0.2 °C and 33.9 ± 0.7% respectively.
- Samples were not dried, and were wrapped in plastic film to avoid moisture evaporation from AAM samples over the course of the test. Some moisture is required as the charge moves by ionic conductivity within AAM sensors [8].
- Loading rates were kept constant.

4.3.2. Loading schemes

Fig. 12 summarises the mechanical testing conducted in this work. Large scale concrete cubes (sample set 2.2B in Fig. 12) were tested using a 500 kN capacity load-controlled compressive tester with 0.2 kN precision. The loading rate was 5 kN/s. All remaining sample sets (1.1, 1.2, 2.1A, and 2.2A) were tested using a displacement-controlled universal tester. The displacement rate applied was fixed at 0.3 mm/min. A small preload was applied to all samples to eliminate any nonlinearity issues that commonly occur at low loads [58].

For concrete compressive testing, electrically insulating GFRP sheets were placed between the loading plates and the sample to avoid making the compressive tester part of the electrical circuit.

As shown in Fig. 12, the strain sensing investigation was divided into an initial investigation (part 1) and the in-depth investigation (part 2). In part 1, the responses of printed AAM sensors were investigated under compression and tension using GFRP test pieces. In part 2, compressive strain responses were investigated using concrete cubes, and tensile strain responses were investigated in more detail using GFRP test pieces.

The experiments summarised in Fig. 12 made use of up to three time-dependent loading profiles, described as follows:

- **Segment 1 (stepped).** Samples were loaded in 5-step increments and then unloaded in 5-step increments. Each step was held for 1 min to allow impedance measurements to be taken. This loading cycle was repeated 6 times overall. For large concrete cubes under load-controlled compressive testing (sample set 2.1A), the step size was 10 kN and the maximum load was 50 kN. For displacement-controlled compressive tested samples, the step size was 0.02 mm and the maximum displacement was 0.1 mm. For tensile tested samples, the maximum displacement was 0.04 mm with a step size of 0.008 mm. All of the maximum values keep sample substrates within their linear-elastic regions.
- **Segment 2 (cycling).** Samples were cycled 40 times without steps between the minimum and maximum ranges of displacement described for Segment 1. Impedance measurements were not taken.
- **Segment 3 (stepped).** The Segment 1 loading pattern and measurement protocol were repeated after cycling.

5. Strain sensing results and discussion

5.1. GFRP substrate strain sensing

Fig. 13 shows time series of the fractional change in electrical impedance modulus, $\Delta Z/Z$, for AAM patches adhered to GFRP test pieces under tension and compression (sample sets 1.1 and 1.2 in Fig. 12 respectively). The dynamic response of the impedance aligns with the expected behaviour of AAMs in both loading directions, but the repeatability and reversibility are clearly low, with the baseline impedance of samples at zero load increasing with each load cycle.

Reversible behaviour is difficult to achieve in cementitious sensors due to small changes in the microstructure of the matrix after a load is applied [53,59]. However, it has been found that reversibility and repeatability can be improved by imposing multiple load cycles on a sample prior strain characterisation [57]. Fig. 14 presents the tensile strain sensing behaviour for an AAM patch adhered to GFRP under tension (sample set 2.2A). The responses during loading Segment 1 (prior to cyclic loading) and Segment 3 (post cyclic loading) are shown. Similar to Fig. 13, these samples show repeatability issues during loading Segment 1, but repeatability improved after cycling loading. This suggests that there may need to be a period of "breaking in" or relaxation prior to using these sensors for structural health monitoring in the field.

Fig. 15 presents the impedance response for a GFRP sample post-cycling as a function of applied displacement. The observed hysteresis phenomenon has been seen in cementitious strain sensors in previous studies [10,15], but it is often underreported and its root causes are still not well understood. Fig. 16 presents the averaged impedance response of Fig. 15 as a function of applied strain. As shown, the gauge factor (GF) for this sample was 14.42.

While cyclic loading has made the repeatability acceptable within each sample, the repeatability *between* individual GFRP samples was low. Of the 5 samples tested, gauge factors ranged from 14 to 65. This may be due to the inconsistent strain transfer imparted by the manually-deployed sand-epoxy layer. Overall, a high variation in GFs is common in filler-free AAM sensors, with reported gauge factors in other studies ranging from 20 to 2000 [10,56,60,61]. The fundamental reason could lie in strain's influence on ion exchange and conductivity in AAM, but while studies have been carried out [6,8,62], this concept is not understood to the extent where sensing performance of AAM binders can be reliably predicted. Further work in this field is required.

Finally, Fig. 17 displays the sensing response for the instrumented GFRP under high levels of tensile strain. The behaviour is nonlinear as expected [63], as applying high loads compromises the structural integrity of the AAM patches, leading to cracking and debonding.

5.2. Concrete strain sensing: compression

5.2.1. 50 mm cubes

Fig. 18 presents the strain sensing response for 50 mm concrete cubes

under compression (2.1A in Fig. 12). Similar to GFRP test pieces, there are repeatability issues during Segment 1 that can be explained by minor damage in the patch, and the development (and gradual relaxation) of stresses at the interface between the substrate and the overlay upon each cycle [53]. After undergoing cyclic loading in Segment 2, sensing performance is more stable.

Fig. 19 presents the fractional change in impedance as a function of applied displacement for all six load cycles in Segment 3. The 3D printed sensing patches again showcase hysteresis. GFs between samples were reasonably repeatable at 8.59 ± 1.55. This is a better repeatability than that typical found for filler-free applications reported by other authors, where GFs range between 20 and 65 [10,60,64]. This may be because of the improved repeatability offered by the 3D printing process. The mean GF is lower than these previous studies, and this may also be a direct consequence of 3D printing, as we have found that it results in a lower adhesion strength between materials (see Section 5.3), and hence a lower strain transfer.

5.2.2. 100 mm cubes

Changes in impedance were found to be consistent for patches printed onto 100 mm side concrete cubes under loading. As displacement measurements were not acquired with this loading apparatus, the stress sensitivity coefficient (SSC) was used to characterise the sensing performance of the patches. Analogous to the gauge factor, this is defined as the fractional change in impedance per unit applied stress. Fig. 20 shows an average SSC for one sample of -0.046 MPa^{-1}. The average SSC over all 3 samples tested was -0.034 ± 0.008 MPa^{-1}.

5.3. 3D Printing: effect on strain sensing

To authors' knowledge, the effect of 3D printing on self-sensing cement strain sensing performance has never been studied. However, we can draw analogues with mechanical performance: for instance, it is known that printed cementitious materials present anisotropic mechanical behaviour due to the weakened interface between layers and are thus affected by the direction of the applied load in comparison to the direction of layers [46,65]. In the present work, AAM patches were printed following a 90^{o} crosshatched infill pattern (the first layer is deposited vertically, second layer horizontally). This was done to create a more uniform patch that would be less sensitive to directional effects.

The printed AAM was also highly workable to improve adhesion with the concrete substrate, and interlayer adhesion between subsequently extruded material lines. Recent studies have also stated that the rheological properties of a mix play a more important role on the mechanical performance of printed binders rather the printing orientation compared to the applied load [66]. From this we can tentatively suggest that strain transfer has been optimised to some extent given the current set up, but more study of this area is required.

5.4. Sensitivity to electrode orientation

Finally, the strain sensing performance was investigated as a function of the electrode layout. Referring to Fig. 10b, electrodes were connected using Layout 2 and the 100 mm cube test experiment (sample set 2.2B) was repeated. As shown in Fig. 21, even though the sample is under compression, the impedance increased (i.e. tensile strain was measured) with an SSC of 0.014 MPa^{-1}. This value for the SSC is about 30% of the value noted for Layout 1 in Fig. 20, suggesting that the patch may now be measuring strains resulting from the Poisson effect. Further studies will be required to investigate whether this is truly the case, but it is clear that the sensitivity to strain in one direction can be reduced by swapping the electrode layout. This may be a useful technique for reference sensing in future.

5.5. Sensor evaluation and potential improvements

The GFs for the AAM sensors in this study ranged from 8 to 60. Incorporating conductive filler such as carbon fiber [57] and graphene [67] has shown to be able increase the strain sensitivity of AAM sensors. One of the drawbacks of incorporating such filler, as mentioned in Section 3.1, is that extrudability of the mix will be compromised. As such proper consideration must be given when selecting conductive filler under printing applications. That said rather than adding conductive filler, an effective means of increasing the GF in sensing coatings would be by increasing the bond between the sensor and the substrate as the performance is influenced by the bond achieved [18]. Adhesion between the sensor and the concrete substrate was relatively low (0.6 MPa), therefore it can be assumed that only a portion of strain is being successfully detected. The bond strength can be improved by applying a more aggressive surface preparation technique such as sandblasting [47]. This will enable a higher bond strength which in turn will allow a high degree of strain to be transferred from the substrate to the sensor.

It should be pointed out that in this study, the temperature and the moisture content of the sensor were controlled during testing. The strain sensing response of cementitious materials may vary if these factors are changed [68]. Future work is required to investigate the impact of these conditions on AAM strain sensing.

6. Conclusions

This paper presented experimental protocols for comparing and optimising 3D printed cement repairs. The adhesion strength between the printed patches and concrete substrates was 0.6 MPa, which is within the range required for a non-structural concrete repair. Alkali-activated material coatings were then printed onto concrete cubes and glass fibre reinforced polymer sheets, and their strain-sensing responses were investigated under compression and tension. These printed self-sensing cements exhibit a strain-dependent electrical impedance response without relying on the use of conductive fillers, and showcase a linear response at low loads. The sensors required multiple loading cycles before a repeatable strain response was achieved, and demonstrated hysteretic effects. Gauge factors for the sensors ranged from 8 to 60, with 3D printed patches on concrete substrates showing a high level of repeatability between samples. Future work will look to take this printing process out a gantry 3D printer so that strain sensing patches can be deployed more flexibly using extruders mounted to robotic arms.

Declaration of Competing Interest

None.

Acknowledgements

This work was funded by the Royal Society (RG160748), the Scottish Funding Council's Oil & Gas Innovation Centre, and the Engineering and Physical Sciences Council (EPSRC, EP/T023198/1).

References

[1] S. Ding, S. Dong, A. Ashour, B. Han, Development of sensing concrete: principles, properties and its applications, J. Appl. Phys. 126 (2019), https://doi.org/10.1063/1.5128242.
[2] X. Li, M. Li, Multifunctional self-sensing and ductile cementitious materials, Cem. Concr. Res. 123 (2019), 105714, https://doi.org/10.1016/j.cemconres.2019.03.008.
[3] J. McAlorum, M. Perry, C. Vlachakis, L. Biondi, B. Lavoie, Robotic spray coating of self-sensing metakaolin geopolymer for concrete monitoring, Autom. Constr. 121 (2021), 103415, https://doi.org/10.1016/j.autcon.2020.103415.
[4] J. McAlorum, M. Perry, A.C. Ward, C. Vlachakis, Concreits: an electrical impedance interrogator for concrete damage detection using self-sensing repairs, Sensors 21 (2021), https://doi.org/10.3390/s21217081.

[5] C. Vlachakis, M. Perry, L. Biondi, J. Mcalorum, 3D printed temperature-sensing repairs for concrete structures, Additiv. Manuf. 34 (2020), 101238, https://doi.org/10.1016/j.addma.2020.101238.

[6] L. Biondi, M. Perry, J. McAlorum, C. Vlachakis, A. Hamilton, Geopolymer-based moisture sensors for reinforced concrete health monitoring, Sensors Actuators B Chem. 309 (2020), 127775, https://doi.org/10.1016/j.snb.2020.127775.

[7] M. Saafi, A. Gullane, B. Huang, H. Sadeghi, J. Ye, F. Sadeghi, Inherently multifunctional geopolymeric cementitious composite as electrical energy storage and self-sensing structural material, Compos. Struct. 201 (2018) 766–778, https://doi.org/10.1016/j.compstruct.2018.06.101.

[8] C. Lamuta, S. Candamano, F. Crea, L. Pagnotta, Direct piezoelectric effect in geopolymeric mortars, Mater. Des. 107 (2016) 57–64, https://doi.org/10.1016/j.matdes.2016.05.108.

[9] X.M. Cui, G.J. Zheng, Y.C. Han, F. Su, J. Zhou, A study on electrical conductivity of chemosynthetic Al2O3-2SiO2geoploymer materials, J. Power Sources 184 (2008) 652–656, https://doi.org/10.1016/j.jpowsour.2008.03.021.

[10] A. D'Alessandro, D. Coffetti, E. Crotti, L. Coppola, A. Meoni, F. Ubertini, Self-sensing properties of green alkali-activated binders with carbon-based nanoinclusions, Sustainability 12 (2020) 9916, https://doi.org/10.3390/su12239916.

[11] M. Abedi, R. Fangueiro, A.C. Gomes, Ultra-sensitive affordable cementitious composite with high mechanical and microstructural performances by hybrid CNT/GNP, Materials 13 (2020) 3484, https://doi.org/10.3390/ma13163484.

[12] S. Sun, S. Ding, B. Han, S. Dong, X. Yu, D. Zhou, J. Ou, Multi-layer graphene-engineered cementitious composites with multifunctionality/intelligence, Compos. Part B 129 (2017) 221–232, https://doi.org/10.1016/j.compositesb.2017.07.063.

[13] B. Han, J. Ou, Embedded piezoresistive cement-based stress/strain sensor, Sensors Actuators A Phys. 138 (2007) 294–298, https://doi.org/10.1016/j.sna.2007.05.011.

[14] S. Ding, Y. Ruan, X. Yu, B. Han, Y. Ni, Self-monitoring of smart concrete column incorporating CNT/NCB composite fillers modified cementitious sensors, Constr. Build. Mater. 201 (2019) 127–137, https://doi.org/10.1016/j.conbuildmat.2018.12.203.

[15] Y. Wang, Y. Wang, B. Han, B. Wan, G. Cai, Z. Li, Strain monitoring of concrete components using embedded carbon nanofibers/epoxy sensors, Constr. Build. Mater. 186 (2018) 367–378, https://doi.org/10.1016/j.conbuildmat.2018.07.147.

[16] F.J. Baeza, O. Galao, E. Zornoza, P. Garcés, Multifunctional cement composites strain and damage sensors applied on reinforced concrete (rc) structural elements, Materials 6 (2013) 841–855, https://doi.org/10.3390/ma6030841.

[17] M. Perry, M. Saafi, G. Fusiek, P. Niewczas, Hybrid optical-fibre/geopolymer sensors for structural health monitoring of concrete structures, Smart Mater. Struct. 24 (2015), 045011, https://doi.org/10.1088/0964-1726/24/4/045011.

[18] M. Gerber, C. Weaver, L.E. Aygun, N. Verma, J.C. Sturm, B. Glišić, Strain transfer for optimal performance of sensing sheet, Sensors 18 (2018) 1–16, https://doi.org/10.3390/s18061907.

[19] J. Manuel, D. Delgado, L. Oyedele, A. Ajayi, L. Akanbi, O. Akinade, M. Bilal, H. Owolabi, Robotics and automated systems in construction : understanding industry- specific challenges for adoption, J. Building Eng. 26 (2019), 100868, https://doi.org/10.1016/j.jobe.2019.100868.

[20] C. Wong, E. Yang, X.-T. Yan, D. Gu, Autonomous robots for harsh environments: a holistic overview of current solutions and ongoing challenges, systems Science & Control, Engineering 6 (2018) 213–219, https://doi.org/10.1080/21642583.2018.1477634.

[21] M.A. Hossain, A. Zhumabekova, S.C. Paul, J.R. Kim, A review of 3D printing in construction and its impact on the labor market, Sustainability 12 (2020) 8492, https://doi.org/10.3390/su12208492.

[22] M. Mohammad, E. Masad, S.G. Al-Ghamdi, 3D concrete printing sustainability: a comparative life cycle assessment of four construction method scenarios, Buildings 10 (2020) 245, https://doi.org/10.3390/buildings10120245.

[23] J.L. Provis, S.A. Bernal, Geopolymers and related alkali-activated materials, Annu. Rev. Mater. Res. 44 (2014) 299–327, https://doi.org/10.1146/annurev-matsci-070813-113515.

[24] E. García-Macías, A. D'Alessandro, R. Castro-Triguero, D. Pérez-Mira, F. Ubertini, Micromechanics modeling of the uniaxial strain-sensing property of carbon nanotube cement-matrix composites for SHM applications, Compos. Struct. 163 (2017) 195–215, https://doi.org/10.1016/j.compstruct.2016.12.014.

[25] C. Zanotti, P.H.R. Borges, A. Bhutta, N. Banthia, Bond strength between concrete substrate and metakaolin geopolymer repair mortar: effect of curing regime and PVA fiber reinforcement, Cem. Concr. Compos. 80 (2017) 307–316, https://doi.org/10.1016/j.cemconcomp.2016.12.014.

[26] S. Chaves Figueiredo, C. Romero Rodríguez, Z.Y. Ahmed, D.H. Bos, Y. Xu, T. M. Salet, O. Çopuroğlu, E. Schlangen, F.P. Bos, An approach to develop printable strain hardening cementitious composites, Materials and Design 169 (2019), 107651, https://doi.org/10.1016/j.matdes.2019.107651.

[27] B. Zareiyan, B. Khoshnevis, Effects of interlocking on interlayer adhesion and strength of structures in 3D printing of concrete, Autom. Constr. 83 (2017) 212–221, https://doi.org/10.1016/j.autcon.2017.08.019.

[28] T.T. Le, S.A. Austin, S. Lim, R.A. Buswell, A.G.F. Gibb, T. Thorpe, Mix design and fresh properties for high-performance printing concrete, Materials and Structures/Materiaux et Constructions 45 (2012) 1221–1232, https://doi.org/10.1617/s11527-012-9828-z.

[29] A. Kazemian, X. Yuan, E. Cochran, B. Khoshnevis, Cementitious materials for construction-scale 3D printing: laboratory testing of fresh printing mixture, Constr. Build. Mater. 145 (2017) 639–647, https://doi.org/10.1016/j.conbuildmat.2017.04.015.

[30] British Standards Institution, BS EN 196–3:2016 Methods of testing cement. Part 3: Determination of setting time and soundness, London, 2016.

[31] B. Panda, C. Unluer, M.J. Tan, Extrusion and rheology characterisation of geopolymer nanocomposites used in 3D printing, Compos. Part B 176 (2019), https://doi.org/10.1016/j.compositesb.2019.107290.

[32] M. Chougan, S. Hamidreza Ghaffar, M. Jahanzat, A. Albar, N. Mujaddedi, R. Swash, The influence of nano-additives in strengthening mechanical performance of 3D printed multi-binder geopolymer composites, Constr. Build. Mater. 250 (2020), 118928, https://doi.org/10.1016/j.conbuildmat.2020.118928.

[33] B.N. Diggs-McGee, E.L. Kreiger, M.A. Kreiger, M.P. Case, Print time vs. elapsed time: a temporal analysis of a continuous printing operation for additive constructed concrete, Additive Manuf. 28 (2019) 205–214, https://doi.org/10.1016/j.addma.2019.04.008.

[34] M. Chen, L. Li, J. Wang, Y. Huang, S. Wang, P. Zhao, L. Lu, X. Cheng, Rheological parameters and building time of 3D printing sulphoaluminate cement paste modified by retarder and diatomite, Constr. Build. Mater. 234 (2020), https://doi.org/10.1016/j.conbuildmat.2019.117391.

[35] S.A.O. Nair, H. Alghamdi, A. Arora, I. Mehdipour, G. Sant, N. Neithalath, Linking fresh paste microstructure, rheology and extrusion characteristics of cementitious binders for 3D printing, J. Am. Ceram. Soc. 102 (2019) 3951–3964, https://doi.org/10.1111/jace.16305.

[36] B. Panda, M.J. Tan, Experimental study on mix proportion and fresh properties of fly ash based geopolymer for 3D concrete printing, Ceram. Int. 44 (2018) 10258–10265, https://doi.org/10.1016/j.ceramint.2018.03.031.

[37] C. Joh, J. Lee, T.Q. Bui, J. Park, I.-H. Yang, Buildability and mechanical properties of 3D printed concrete, Materials 13 (2020) 4919, https://doi.org/10.3390/ma13214919.

[38] V.N. Nerella, M. Krause, V. Mechtcherine, Direct printing test for buildability of 3D-printable concrete considering economic viability, Autom. Constr. 109 (2020), 102986, https://doi.org/10.1016/j.autcon.2019.102986.

[39] L. Courard, R. Degeimbre, A capillary action test for the investigation of adhesion in repair technology, Can. J. Civ. Eng. 30 (2004) 1101–1110, https://doi.org/10.1139/l03-061.

[40] D. Jon Leech, W. Guy, S. Klein, The polychromatic woodburytype—colour tracking in translucent, patterned gelatin/pigment films, Molecules 25 (2020), https://doi.org/10.3390/molecules25112468.

[41] R.J.M. Wolfs, F.P. Bos, T.A.M. Salet, Hardened properties of 3D printed concrete: the influence of process parameters on interlayer adhesion, Cem. Concr. Res. 119 (2019) 132–140, https://doi.org/10.1016/j.cemconres.2019.02.017.

[42] L. Courard, T. Piotrowski, A. Garbacz, Near-to-surface properties affecting bond strength in concrete repair, Cem. Concr. Compos. 46 (2014) 73–80, https://doi.org/10.1016/j.cemconcomp.2013.11.005.

[43] D.R. Morgan, Compatibility of concrete repair materials and systems, Constr. Build. Mater. 10 (1996) 57–67, https://doi.org/10.1016/0950-0618(95)00060-7.

[44] British Standards Institution, Products and systems for the protection and repair of concrete structures - Test methods - Measurement of bond strength by pull-off, 1999.

[45] V.A. Nunes, P.H.R. Borges, C. Zanotti, Mechanical compatibility and adhesion between alkali-activated repair mortars and Portland cement concrete substrate, Constr. Build. Mater. 215 (2019) 569–581, https://doi.org/10.1016/j.conbuildmat.2019.04.189.

[46] S.H. Bong, B. Nematollahi, A. Nazari, M. Xia, J. Sanjayan, Method of optimisation for ambient temperature cured sustainable geopolymers for 3D printing construction applications, Materials 12 (2019) 902, https://doi.org/10.3390/ma12060902.

[47] P.M.D. Santos, N.B.S. Julio, Comparison of methods for texture assessment of concrete surfaces, ACI Mater. J. 107 (2011) 433–440.

[48] L.J. van der Pauw, A method of measuring specific resistivity and and hall effect of discs of arbitrary shape, Philips, Research Reports 13 (1958) 1–9.

[49] Y. Yao, X. Duan, J. Luo, T. Liu, Two-probe versus van der Pauw method in studying the piezoresistivity of single-wall carbon nanotube thin films, Nanotechnology 28 (2017), https://doi.org/10.1088/1361-6528/aa8585.

[50] F. Azhari, N. Banthia, Cement-based sensors with carbon fibers and carbon nanotubes for piezoresistive sensing, Cem. Concr. Compos. 34 (2012) 866–873, https://doi.org/10.1016/j.cemconcomp.2012.04.007.

[51] Y. Hong, Z. Li, G. Qiao, J. Ou, W. Cheng, Pressure sensitivity of multiscale carbon-admixtures–enhanced cement-based composites, Nanomat. Nanotechnol. 8 (2018) 1–8, https://doi.org/10.1177/1847980418793529.

[52] Y. Hong, Z. Li, G. Qiao, J. Ou, W. Cheng, Pressure sensitivity of multiscale carbon-admixtures–enhanced cement- based composites, Nanomat. Nanotechnol. 8 (2018) 1–8, https://doi.org/10.1177/1847980418793529.

[53] M.Q. Sun, R.J.Y. Liew, M.H. Zhang, W. Li, Development of cement-based strain sensor for health monitoring of ultra high strength concrete, Constr. Build. Mater. 65 (2014) 630–637, https://doi.org/10.1016/j.conbuildmat.2014.04.105.

[54] H. Siad, M. Lachemi, M. Sahmaran, H.A. Mesbah, K.A. Hossain, Advanced engineered cementitious composites with combined self-sensing and self-healing functionalities, Constr. Build. Mater. 176 (2018) 313–322, https://doi.org/10.1016/j.conbuildmat.2018.05.026.

[55] W. Dong, W. Li, N. Lu, F. Qu, K. Vessalas, D. Sheng, Piezoresistive behaviours of cement-based sensor with carbon black subjected to various temperature and water content, Compos. Part B 178 (2019), https://doi.org/10.1016/j.compositesb.2019.107488.

[56] Y. Ma, W. Liu, J. Hu, J. Fu, Z. Zhang, H. Wang, Optimization on the piezoresistivity of alkali-activated fly ash/slag mortar by using conductive aggregates and carbon fibers, Cem. Concr. Compos. 114 (2020), 103735, https://doi.org/10.1016/j.cemconcomp.2020.103735.

[57] L. Deng, Y. Ma, J. Hu, S. Yin, X. Ouyang, J. Fu, A. Liu, Z. Zhang, Preparation and piezoresistive properties of carbon fiber-reinforced alkali-activated fly ash/slag mortar, Constr. Build. Mater. 222 (2019) 738–749, https://doi.org/10.1016/j.conbuildmat.2019.06.134.
[58] O. Galao, F.J. Baeza, E. Zornoza, P. Garcés, Strain and damage sensing properties on multifunctional cement composites with CNF admixture, Cem. Concr. Compos. 46 (2014) 90–98, https://doi.org/10.1016/j.cemconcomp.2013.11.009.
[59] Z. Tian, Y. Li, J. Zheng, S. Wang, A state-of-the-art on self-sensing concrete: Materials, fabrication and properties, Composites Part B 177 (2019), 107437, https://doi.org/10.1016/j.compositesb.2019.107437.
[60] M. Saafi, L. Tang, J. Fung, M. Rahman, F. Sillars, J. Liggat, X. Zhou, Graphene/fly ash geopolymeric composites as self-sensing structural materials, Smart Mater. Struct. 23 (2014), 065006, https://doi.org/10.1088/0964-1726/23/6/065006.
[61] C. Lamuta, L. Bruno, S. Candamano, L. Pagnotta, Piezoresistive characterisation of graphene/metakaolin based geopolymeric mortar composites, MRS Advances 2 (2017) 3773–3779, https://doi.org/10.1557/adv.2017.595.
[62] T. Skorina, Ion exchange in amorphous alkali-activated aluminosilicates: potassium based geopolymers, Appl. Clay Sci. 87 (2014) 205–211, https://doi.org/10.1016/j.clay.2013.11.003.
[63] D.-Y. Yoo, S. Kim, S.H. Lee, Self-sensing capability of ultra-high-performance concrete containing steel fibers and carbon nanotubes under tension, Sensors Actuators A Phys. 276 (2018) 125–136, https://doi.org/10.1016/j.sna.2018.04.009.
[64] P. Rovnaník, I. Kusák, P. Bayer, P. Schmid, L. Fiala, Comparison of electrical and self-sensing properties of Portland cement and alkali-activated slag mortars, Cem. Concr. Res. 118 (2019) 84–91, https://doi.org/10.1016/j.cemconres.2019.02.009.
[65] B. Panda, S.C. Paul, L.J. Hui, Y.W.D. Tay, M.J. Tan, Additive manufacturing of geopolymer for sustainable built environment, J. Clean. Prod. 167 (2017) 281–288, https://doi.org/10.1016/j.jclepro.2017.08.165.
[66] D. Heras Murcia, M. Genedy, M.M. Reda Taha, Examining the significance of infill printing pattern on the anisotropy of 3D printed concrete, Construction and Building Materials 262 (2020), 120559, https://doi.org/10.1016/j.conbuildmat.2020.120559.
[67] S. Candamano, E. Sgambitterra, C. Lamuta, L. Pagnotta, S. Chakraborty, F. Crea, Graphene nanoplatelets in geopolymeric systems: a new dimension of nanocomposites, Mater. Lett. 236 (2019) 550–553, https://doi.org/10.1016/j.matlet.2018.11.022.
[68] E. Demircilioğlu, E. Teomete, E. Schlangen, F.J. Baeza, Temperature and moisture effects on electrical resistance and strain sensitivity of smart concrete, Constr. Build. Mater. 224 (2019) 420–427, https://doi.org/10.1016/j.conbuildmat.2019.07.091.